Evaluation of three analytical methods for reconstruction from cone-beam data on a short circular scan

Frank Dennerlein, *Graduate Student Member, IEEE,* Frédéric Noo, *Member, IEEE,*
Stefan Hoppe, *Graduate Student Member, IEEE,* Joachim Hornegger, and Günter Lauritsch

***Abstract*— This article focuses on the problem of three-dimensional image reconstruction from cone-beam data acquired along a partial circular scan (short-scan): We present a detailed comparative evaluation of three state-of-the-art analytical algorithms suggested to achieve image reconstruction in this short-scan geometry. Our evaluation involves quantitative studies, such as the estimation of the contrast-to-noise performance, of the achievable spatial resolution and of the cone-beam artifact behavior of these reconstruction algorithms. In addition to that, we also provide a visual assessment of image quality by evaluating reconstructions of the FORBILD head phantom and a disc phantom. The numerical results presented in this paper were obtained using computer-simulated cone-beam data, while focusing on non-truncated projection data and geometry parameters that are similar to those of real medical C-arm devices.**

I. Introduction

Three-dimensional (3D) image reconstruction from cone-beam (CB) projection data measured on a short circular scan is an important problem in medical imaging. Unfortunately, this problem cannot in general be solved to provide results that are simultaneously accurate and stable. This is due to the data set being incomplete: a short circular scan only satisfies Tuy's sufficiency condition [1] in the plane of the source motion. Numerous algorithms have been suggested for approximate reconstruction, each responding differently to the missing data and also to data noise. On the other hand, however, few comparison studies have been published.

In this work, we present a detailed comparative evaluation of three competitive state-of-the-art analytical reconstruction algorithms, namely the short-scan FDK-method [2], the ACE-method [3] and the DBP method [4]. The evaluation includes both, qualitative and quantitative figures-of-merit, and is based on computer-simulated CB data of three analytically defined phantoms: the FORBILD head phantom, a CB performance phantom and a disc phantom.

Manuscript received May 11, 2007. This work was partially supported by a grant of Siemens AG, Medical Solutions and by the U.S. National Institutes of Health (NIH) under grant R01 EB000627. Its contents are solely the responsibility of the authors and do not necessarily represent the official views of the NIH.

F. Dennerlein (fdenner@ucair.med.utah.edu) and F. Noo are with the Department of Radiology (UCAIR), University of Utah, Salt Lake City, UT, USA.

S. Hoppe and J. Hornegger are with the Institute of Pattern Recognition, University of Erlangen-Nuremberg, Erlangen, Germany.

G. Lauritsch is with Siemens AG, Medical Solutions, Forchheim, Germany.

Our work is presented in the following order. In Sec. II, we introduce briefly the reconstruction problem in the short-scan circular acquisition geometry. The algorithmic steps of the three considered reconstruction approaches are described in Sec. III. In Sec. IV, we compare these reconstruction approaches in terms of spatial resolution, contrast-to-noise ratio and CB artifacts. A visual assessment of image quality achievable with each approach follows in Sec. V. We then present final discussions and conclusions about our work in Sec. VI.

II. Notation and Geometry

In this work, we use $\mathbf{a}(\lambda) = (R\cos\lambda, R\sin\lambda, 0)$ to describe the circular motion of the X-ray source around the object of interest during data acquisition. In this notation, R denotes the radius of the source trajectory and λ corresponds to the polar angle of the source. The CB projections of the object are assumed to be known for λ in the interval $[\lambda_c - \lambda_{ss}/2, \lambda_c + \lambda_{ss}/2]$ with $\lambda_{ss} < 2\pi$. Hence, the center of the scan is at polar angle λ_c, and the CB data cover an angular range of length λ_{ss}; see Fig. 1.

Let $f(\mathbf{x})$ with $\mathbf{x} = (x, y, z)$ denote the spatial density distribution of the interrogated object. The CB projection of this object with the source at polar angle λ is denoted as $g(\lambda, u, v)$, where u and v are Cartesian coordinates defining

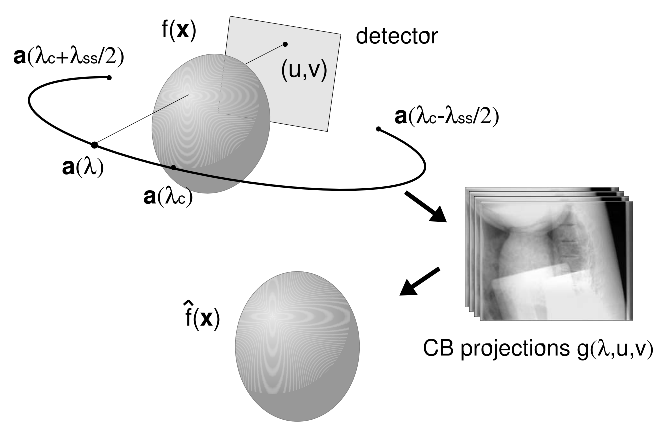

Fig. 1. Illustration of the circular short-scan reconstruction problem. During the scan, the X-ray focus-detector assembly rotates around the object of interest and measures a set of CB projections g. The goal is to compute, from this projection data, an accurate estimate $\hat{f}(\mathbf{x})$ of the function $f(\mathbf{x})$ that represents the spatial distribution of the object density.

the position of pixels in the detector plane. Below, the u-axis is called the horizontal detector coordinate, and we assume that the detector is always oriented so that this axis is parallel to $(\partial/\partial\lambda)\mathbf{a}(\lambda)$.

III. Description of the Algorithms

This section briefly describes the three considered algorithms for image reconstruction from the measured CB projections $g(\lambda, u, v)$.

A. The short-scan FDK method

In the short-scan FDK method [2], the CB projections are first multiplied with the Parker weighting function [5] at fixed v. The outcome is then ramp-filtered in u and backprojected in the original CB geometry with a weight inversely proportional to the square of the source-to-voxel distance. Note that for the numerical evaluations presented in this work, we applied sinc-apodization to the ramp-filter kernel.

B. The ACE method

In the ACE method [3], the CB projections are first differentiated in λ at fixed ray direction, then convolved with the kernel of the Hilbert transform along 3 filter lines per detector point; one of these filter lines is parallel to the u-axis while the other two are oblique and of direction changing with the source position. Once filtered, the data is backprojected in the original CB geometry with a weight inversely proportional to the source-to-voxel distance.

C. The DBP method

The differentiated backprojection (DBP) method follows the approach from [4], in which the CB projections are first multiplied with the Parker weighting function [5] at fixed v, then differentiated in u and finally multiplied with a signum function at fixed v. CB backprojection of this differentiated data with a weight inversely proportional to the square of the source-to-voxel distance and CB backprojection of two boundary terms yields first an intermediate function in the image domain. In a second step, this intermediate function is transformed into the object density estimation $\hat{f}$ using a finite Hilbert inversion along a set of parallel lines in the image domain.

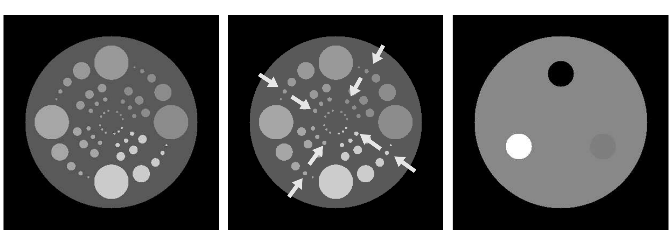

Fig. 2. Two cylinders through the CB performance phantom: (left) cylinder with low-contrast inlays differing from the background by 20HU, 25HU, 30HU and 45HU (grayscale center C=50HU, grayscale width W=100HU); (center) same cylinder with arrows indicating objects used for the resolution evaluation; (right) cylinder with high-contrast inlays (grayscale center C=0HU, grayscale width W=1000HU)

TABLE I

Simulation and Reconstruction Parameters

	Set A	Set B
detector pixel size [mm^2]	0.5×0.5	0.75×0.75
radius of trajectory R [mm]	750	750
distance source-detector D [mm]	750	750
short-scan range [°]	$\lambda_{ss} = 212$	$\lambda_{ss} = 212$
short-scan discretization [°]	$\Delta\lambda = 0.4$	$\Delta\lambda = 0.4$
side length of image voxel [mm]	0.5	0.75

IV. Quantitative Evaluation of Image Quality

In this section, we study the image quality achievable with each of the three reconstruction approaches introduced in section III using quantitative figures-of-merit. Our quantitative evaluations are based on the reconstruction of a modular CB performance phantom that consists of several cylinders embedding each, distinct low- and high-contrast structures. These cylinders are of radius 8 cm, have a background density of 35HU and may be stacked as desired. Two representative slices through the phantom are shown in Fig. 2. CB projections of the performance phantom were simulated using the geometry and discretization parameters described in set A of table I. In the simulation studies, the CB projection of the object was always entirely contained on the detector, i.e. CB projections did not suffer from data truncation issues.

A. Spatial Resolution

Resolution in x and y was first evaluated at $z_0 = 1.5$mm, i.e. near the source-trajectory plane, by placing the CB performance phantom such that the slice shown in Fig. 2 (left)

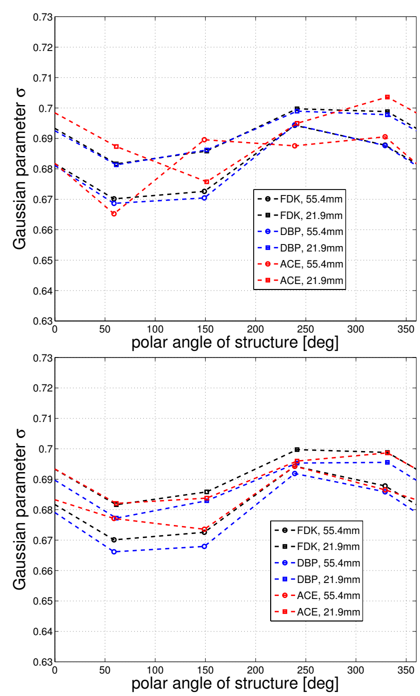

Fig. 3. Resolution parameter σ in pixel units as a function of the polar angle of the circle inlays (FDK - black, DBP - blue, ACE - red). Evaluation (top) close to the plane of the scan ($z_0 = 1.5$mm), (bottom) away from the plane of the scan ($z_0 = 50$mm).

was located at z_0. We focused then on the reconstruction of 8 of the circular inlays of radius 2mm that are in this slice (see arrows in Fig. 2, center). Four of these objects were at 55.4mm from the cylinder center, while the other four were at 21.9mm. We assumed that the (local) loss in spatial resolution at each object location can be modeled by a convolution of the true phantom values with a 2D Gaussian kernel $k(x, y, \sigma)$. This resolution loss was then quantified through the computation of the standard deviation σ of the kernel that minimizes $\|k(x, y, \sigma) * f_l(x, y, z_0) - \hat{f}_l(x, y, z_0)\|_2$. In this expression, f_l ($\hat{f}_l$, resp.) denotes the true (reconstructed, resp.) values of the phantom around one of the 8 circular objects, $*$ denotes a 2D convolution in the coordinates x and y and $\|\cdot\|_2$ denotes the L_2 norm. A large value of σ indicates thus low resolution, since then, the true phantom values need to be strongly smoothed to optimally match the corresponding reconstruction result in a least-square sense.

Next, we investigated the achievable x-y resolution at another location, 50mm away from the plane of the circular scan. To do so, we shifted the CB performance phantom in positive z-direction, such that the slice shown in Fig. 2 (left) was located in the plane $z_0 = 50$mm and repeated the evaluation scheme described in the previous paragraph.

The σ values we obtained close to the source-trajectory plane and away from this plane, while using $\lambda_c = 90°$, are presented in Fig. 3. These results show that, in the investigated regions, the x-y resolution achievable with the FDK method, the DBP method and the ACE method is very similar with a maximum observed difference between these methods of about 1%. With each method, the spatial resolution is in general higher in regions close to the center of the short-scan, i.e. close to the vertex point $\mathbf{a}(\lambda_c)$, than in regions further away from that point; this effect can be observed at $z_0 = 1.5$mm and at $z_0 = 50$mm. Furthermore, the x-y resolution does not seem to depend noticeably on z_0, i.e., the distance to the plane of the scan motion. However, the ACE method appears to have slightly less predicable behavior close to this plane than away from this plane (compare red curves in the top and bottom of Fig. 3). Note that spatial resolution in z direction was not investigated in our evaluation.

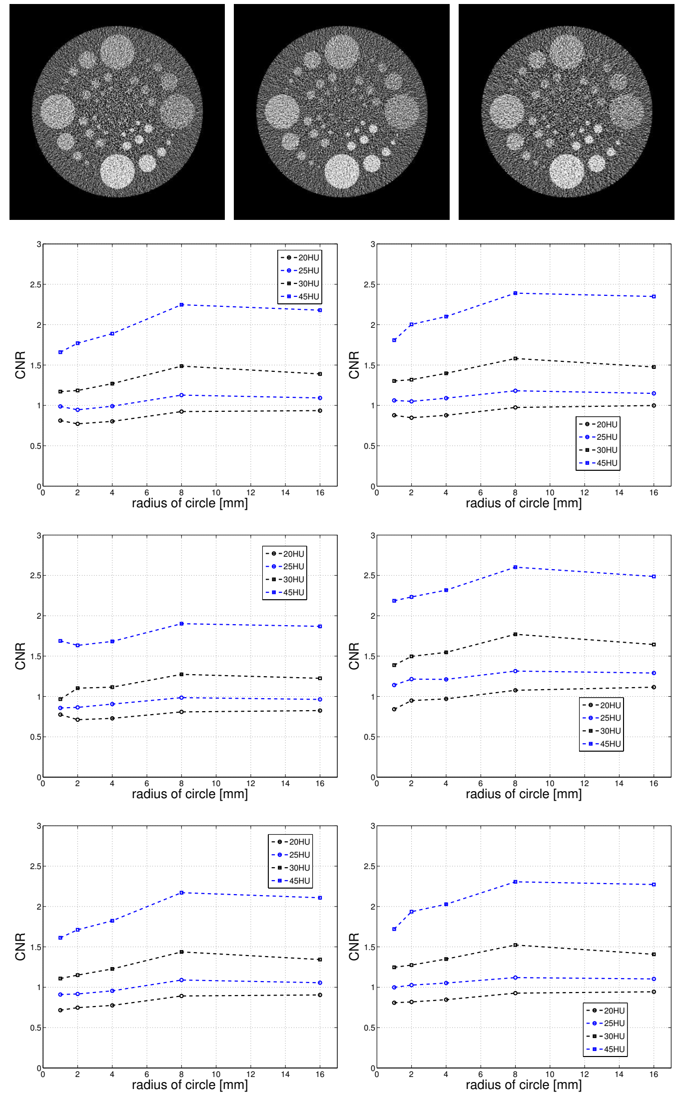

Fig. 5. Evaluation of the CNR. (Top) Reconstructions obtained with (left) short-scan FDK, (middle) ACE and (right) DBP from one noise realization at $z_0 = 1.5$mm in the grayscale window with C=50HU, W=100HU. Bottom: CNR values determined at (left) $z_0 = 1.5$mm and (right) $z_0 = 50$mm as a function of the radius of the low-contrast inlay. In each column, we display first the results for FDK, then for ACE, then for DBP.

B. Contrast to Noise Ratio (CNR)

CNR measurements were performed at two different locations in the image: close to the plane of the source motion (at $z_0 = 1.5$mm) and further away from this plane (at $z_0 = 50$mm). In each case, we placed the performance phantom such that the slice shown in Fig. 2 (left) lies at z_0 and then focused on the reconstructions of the low-contrast inlays in this slice. For each inlay, we defined two regions, as depicted in Fig 4: region A has circular shape and is located entirely inside the inlay, whereas region B contains all points that belong to the cylinder background and that lie inside a ring of thickness 20mm around the inlay. We computed the mean of the reconstructed values in region A and region B to obtain the values $\bar{f}_A$ and $\bar{f}_B$, respectively. The CNR for each inlay was then defined as $(\bar{f}_A - \bar{f}_B)/\sigma_B$, where σ_B denotes the standard deviation of the reconstructed values in B.

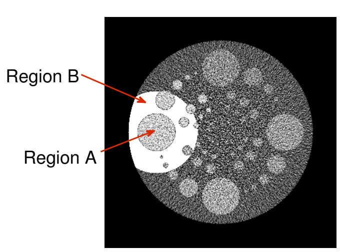

Fig. 4. Illustration of the regions A and B as defined for one low-contrast inlay.

The investigated slice contains 14 inlays for each of the four contrasts listed in the caption of Fig. 2: four inlays are of radius 1mm, 2mm or 4mm, while inlays of radius 8mm and

16mm occur only once. From these 14 inlays, we get 5 CNR values by averaging together the CNR values corresponding to inlays of same radius. This allows the evaluation of the CNR at various levels of resolution and contrast. Experiments were performed using $\lambda_c = 90°$ and CB data with Poisson noise corresponding to $150,000$ photons per ray. This study was carried out for 30 distinct noise realizations; the mean values that we obtained for our CNR figure-of-merit from these 30 noisy data sets are shown in Fig. 5.

As expected, these results show that the CNR is approximately proportional to the density difference between the considered inlay and the background. We also observe that, with each reconstruction approach, the CNR obtained at $z_0 =$ 50mm is better than the CNR at $z_0 = 1.5$mm, with an average increase of about 10%. Considering the results of section IV-A, this gain in CNR is obviously achieved without simultaneously losing x-y resolution. A particularly large difference in the CNR behavior close and off the plane of the circle can be observed with the ACE method: at $z =$ 50mm, ACE yields better CNR than either the short-scan FDK method or the DBP method, while at $z_0 = 1.5$mm, ACE yields lower CNR than these two methods.

C. Cone-Beam Artifacts

CB artifacts were inspected using the cylinder of the performance phantom illustrated in the right of Fig. 2. The inlays in this cylinder have height 16mm, radius 12mm and density -1000HU, 0HU and 1000HU, respectively. The cylinder was positioned such that the bottom of these inlays starts at axial position $z =$ 42mm. A quantification of CB artifacts was achieved by analyzing the reconstructed values within the 3D background region around the inlays, away from their boundary by about 1 pixel. As expected, the reconstructed values were not equal to 35HU, but rather distributed around this true background density. This distribution is here characterized using the mean value and the standard deviation of its histogram. Additionally, we determined the relative frequency of reconstructed pixels in the background, which differed by more than 5HU from the true density (”error pixels”).

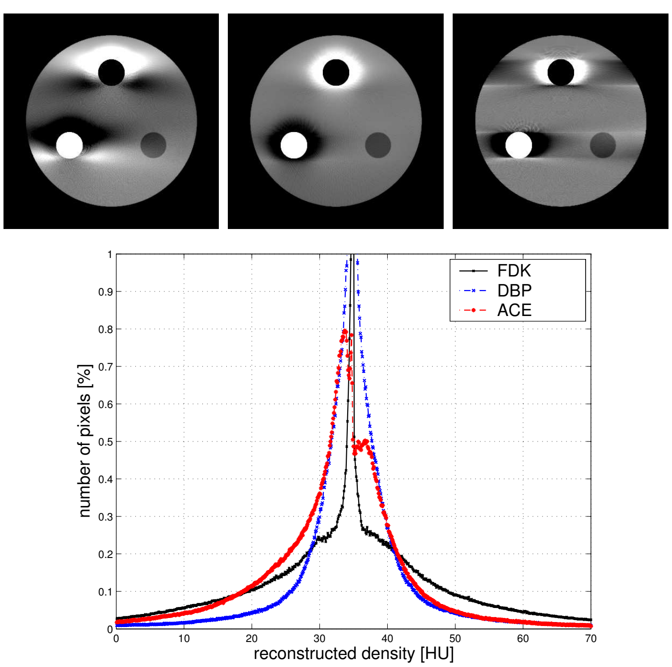

Fig. 6. (Top) Reconstructions at z = 57mm (C=35HU, W=150HU) using (left) FDK, (center) ACE and (right) DBP. (Bottom) Histograms of reconstructed background values (FDK - black, DBP - blue, ACE - red).

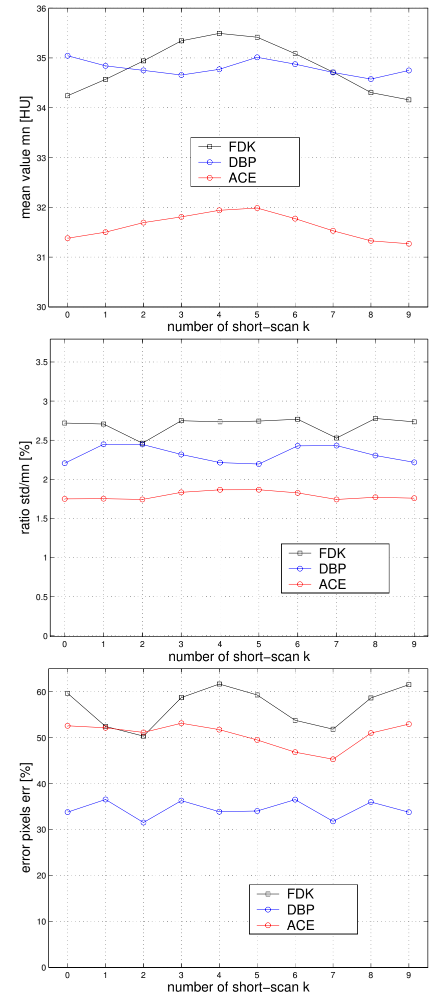

Fig. 7. Histogram parameters for 10 values of λ_c, uniformly distributed over $360°$: (left) mean histogram value (mn), (center) ratio of standard deviation of the histogram to its mean (std/mn), (right) percentage of background voxels with reconstructed error beyond 5HU. For all diagrams: FDK - black, DBP - blue, ACE - red.

Figure 6 shows the slice $z = 50$mm through the reconstructions achieved with the three approaches under comparison. The bottom of this figure shows the corresponding histograms characterizing the distribution of the reconstructed background values. To obtain these results, we centered the short-scan on $\lambda_c = 90°$.

We observe that the histogram corresponding to the FDK method (black curve) decays slower than for DBP and ACE, i.e. FDK yields a larger amount of noticeably wrong pixel densities. The ACE method, on the other hand, seems to underestimate the object densities (the histogram peak is approximately at 32HU) and also yields an unexpected plateau in the density histogram, to the right of the global maximum.

In a second study, we investigated the dependency of CB artifacts on the location of the short-scan relative to the phantom. The graphs in Fig. 7 show the histogram features (mean, standard deviation and error pixels) for 10 different locations of the short scan with $\lambda_c = 90^\circ + k \times 36^\circ$ and $k = 0, 1, ..., 9$. From these results, we note that the position of the short-scan center has seemingly little effect on the magnitude of the CB artifacts. For each position, FDK and DBP yield a good estimate of the mean background density, while ACE underestimates this value by about 3 to 4 units on the HU scale. Also, the relative frequency of error pixels for DBP is approximately 35%, whereas the relative frequency of such pixels for both, FDK and ACE, is between 50% and 60%.

V. Qualitative Evaluation of Image Quality

In this section, image quality is investigated by visual inspection of the reconstructions of two additional, analytically defined phantoms.

We consider first the FORBILD head phantom that is described in [6], and evaluate each algorithm on its capability to recover accurately the low contrast structures inside the head. During the studies, the phantom was shifted by 40 mm in positive z-direction and rotated by 20° about the z-axis in order to break symmetry and to increase the difficulty of the reconstruction problem.

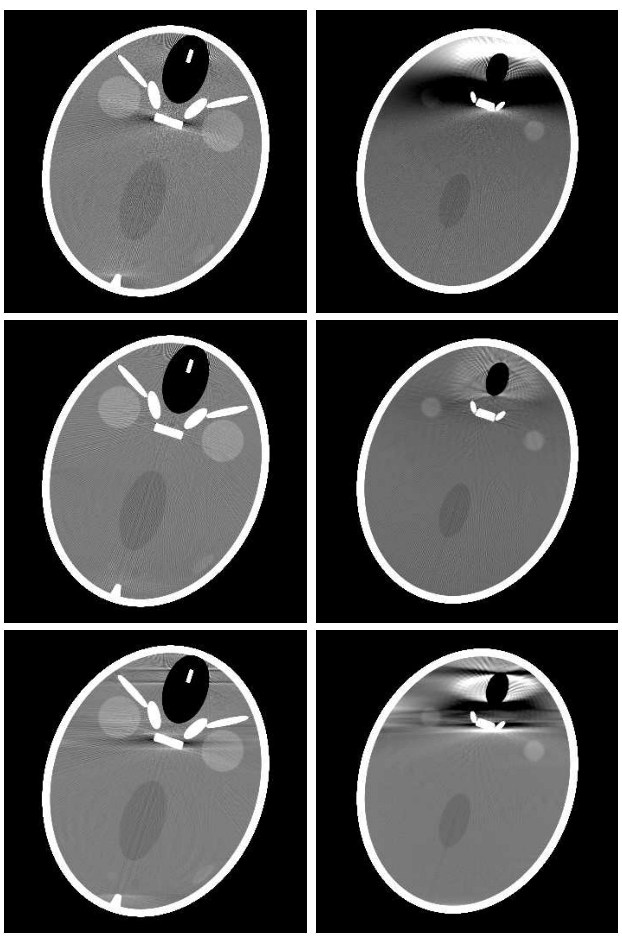

Fig. 8. Slices through the reconstructions of the FORBILD head phantom, at (left) $z = 41.25$ mm and (right) $z = 67.5$ mm. From (top) to (bottom): short-scan FDK, ACE and DBP (C=50HU, W=100HU).

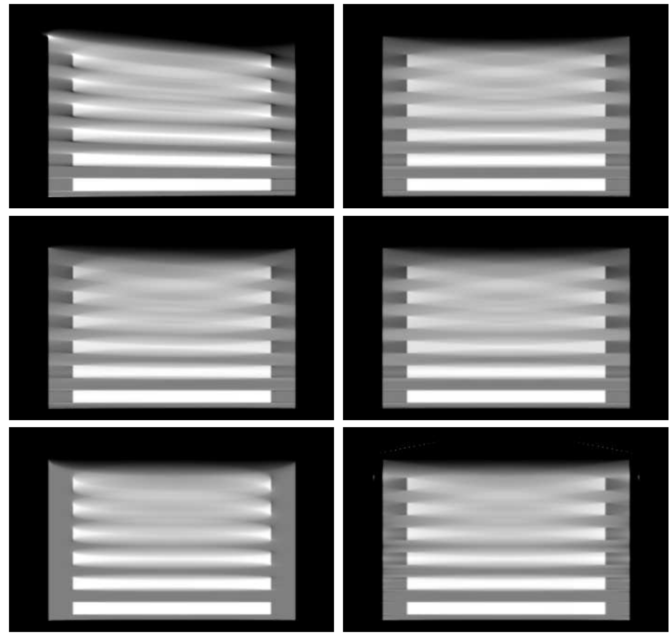

Fig. 9. Central axial slices through the reconstructions of the disk phantom, at (left) $x = 0$ mm and (right) $y = 0$ mm. From (top) to (bottom): short-scan FDK, ACE and DBP. Visualization using C=0HU, W=1000HU.

The second considered phantom consists of 6 cylindrical discs, each of density 500HU, radius 80mm and thickness 10mm. These discs are stacked one above the other, with gaps of 10mm between two adjacent discs, and altogether embedded in a water cylinder of radius 100mm. The phantom is centered at the axis of rotation and shifted, such that the center of its lowest disc is located on the PCS. The reconstruction algorithms were evaluated on their ability to recover the geometric structure of the disc phantom precisely, in particular on their ability to resolve the gaps between the discs and to preserve the symmetry of the phantom.

For both phantoms, non-truncated CB projections were simulated using the geometry parameters described in set B of table I. The slices $z = 41.25$mm and $z = 67.5$mm through the reconstructions of the FORBILD head phantom are shown in Fig. 8, while Fig. 9 presents the reconstructions of the disc phantom on the central, vertical planes $x = 0$mm and $y = 0$mm.

Fig. 8 illustrates that the CB artifacts arising with the short-scan FDK method are typically of smooth shape. However, they have fairly large support and high magnitude and may thus obscure the low-contrast structure inside the head. Compared to FDK, the DBP method yields a noticeable reduction of CB artifacts (see right column of Fig. 8). The remaining artifacts, however, are typically streak-like and may therefore be more easily mistaken with actual object structures when interpreting the reconstruction results. The ACE method can almost entirely avoid CB artifacts for the head phantom study, and yields the best visual image quality in this considered scenario.

The results of Fig. 9 show that short-scan FDK can neither accurately preserve the symmetry of the disc phantom (see slice $x = 0$mm) nor resolve the gaps between the discs that are remote from the plane of the scan motion. ACE also does not allow us to distinguish between the discs at the top of the phantom and cannot avoid shadow-like artifacts in the regions left and right of most discs. The ACE reconstructions in $x = 0$mm and in $y = 0$mm, however, both reflect the phantom symmetry correctly. The CB artifacts arising with the DBP method appear less strong than with either FDK or ACE. The DBP method can reduce (for $y = 0$mm), or entirely overcome (for $x = 0$mm) the shadows enclosing the single discs of the phantom. Furthermore, DBP also preserves the symmetry of the phantom and slightly reduces artifacts between the discs.

VI. Discussion and Conclusion

We have carried out a comparison of three competitive algorithms for reconstruction from CB data on a short circular scan, while considering the geometry parameters representative for medical C-arm devices and non-truncated CB data.

Our studies involved a CB performance phantom, the FORBILD head phantom and a disc phantom and were based on qualitative and quantitative figures of merit. Our results show that each approach seems to have its strengths and weaknesses. We note that FDK is the computationally least complex method, but yields typically a high level of CB artifacts. ACE seems to produce results that are somewhat less quantitative but to provide visually superior image quality when dealing with clinically-relevant phantoms. DBP may produce the most accurate pixel values and may provide the visually best reconstruction of the challenging disc phantom, but occasionally yields disturbing streak artifacts.

We note that the three reconstruction methods we compared in this work have been originally suggested in different contexts and with different goals. The DBP method, for example, can naturally deal with some scenarios of transaxial truncation in the CB projections, in contrast to ACE and FDK. The ACE method, on the other hand, has the nice property to converge towards an efficacious reconstruction algorithm for the full-scan circular trajectory when λ_{ss} approaches $360°$, namely to the full-scan FDK algorithm [2] plus the additional term suggested in [7]. These characteristics are not considered in the comparative study presented in this paper. It would therefore be interesting to evaluate the three reconstruction methods also in different scenarios, considering for instance CB data that are truncated in axial and/or transaxial direction or considering a distinct data acquisition geometry.

Disclaimer

The concepts and information presented in this paper are based on research and are not commercially available.

References

[1] H. K. Tuy, "An inversion formula for cone beam reconstruction," *SIAM J. Appl. Math.*, vol. 43, no. 3, pp. 546–552, 1983.

[2] L. A. Feldkamp, L. C. Davis, and J. W. Kress, "Practical cone-beam algorithm," *J. Opt. Soc. Am. A*, vol. 1, no. 6, pp. 612–619, 1984.

[3] B. E. Nett, T. L. Zhuang, S. Leng, and G. H. Chen, "Arc-based cone-beam reconstruction algorithm using an equal weighting scheme," *J. of X-ray Sci. and Tech.*, vol. 15, no. 1, pp. 19–48, 2007.

[4] L. Yu, Y. Zou, E. Y. Sidky, C. A. Pelizzari, P. Munro, and X. Pan, "Region of interest reconstruction from truncated data in circular cone-beam ct," *IEEE Trans. Med. Imag.*, vol. 25, no. 7, pp. 869–881, 2006.

[5] D. L. Parker, "Optimal short scan convolution reconstruction for fan-beam CT," *Med. Phys.*, vol. 9, no. 2, pp. 254–257, 1982.

[6] "Description of the FORBILD Head Phantom, online at http://www.imp.uni-erlangen.de/forbild/english/results/index.htm."

[7] H. Hu, "An improved cone-beam reconstruction algorithm for the circular orbit," *Scanning*, vol. 18, pp. 572–581, 1996.